Experimental and theoretical study of multinuclear Indium-oxo clusters in CHA zeolite for CH_4 activation at room temperature

Journal:	*Physical Chemistry Chemical Physics*
Manuscript ID	CP-ART-04-2019-001873.R1
Article Type:	Paper
Date Submitted by the Author:	27-Apr-2019
Complete List of Authors:	Maeno, Zen; Hokkaido University, Institute for Catalysis Yasumura, Shunsaku; Hokkaido University, Institute for Catalysis Liu, Chong; Hokkaido University, Institute for Catalysis Toyao, Takashi; Hokkaido University, Institute for Catalysis; Kyoto University, Elements Strategy Initiative for Catalysts and Batteries Kon, Kenichi; Hokkaido University, Institute for Catalysis Nakayama, Akira; Hokkaido University, Institute for Catalysis; JST, PRESTO Hasegawa, Jun-ya; Hokkaido University, Institute for Catalysis Shimizu, Ken-ichi; Hokkaido University, Institute for Catalysis; Kyoto University, Elements Strategy Initiative for Catalysts and Batteries

Experimental and theoretical study of multinuclear indium-oxo clusters in CHA zeolite for CH_4 activation at room temperature

Zen Maeno*[a], Shunsaku Yasumura[a], Chong Liu[a], Takashi Toyao[a,b], Kenichi Kon[a], Akira Nakayama[a,c], Jun-ya Hasegawa[a], Ken-ichi Shimizu*[a,b]

[a] Institute for Catalysis, Hokkaido University, N-21, W-10, Sapporo 001-0021, Japan

[b] Elements Strategy Initiative for Catalysts and Batteries, Kyoto University, Katsura, Kyoto 615-8520, Japan

[c]JST, PRESTO, 4-1-8 Honcho Kawaguchi, Saitama 332-0012, Japan

*Corresponding authors

Zen Maeno, Ken-ichi Shimizu

E-mail: kshimizu@cat.hokudai.ac.jp, TEL: +81-11-706-9164

†Electronic Supplementary Information (ESI) available: See DOI: 10.1039/x0xx00000x.

Abstract: We have carried out an experimental and theoretical study of CHA-zeolite supported indium (In)-oxo clusters that promote CH_4 activation at room temperature. X-ray absorption fine structure (XAFS) measurements indicate the formation of multinuclear In-oxo clusters by the O_2 activation of the In(I)-exchanged CHA zeolite prepared through reductive solid-state ion exchange (RSSIE). The structure of the In-oxo clusters and their locations were investigated in detail using *ab initio* thermodynamic analysis. The redox properties of the In species during RSSIE and the formation of the In-oxo clusters were also studied by temperature programmed reaction and *in situ* XAFS measurements. The reaction of CH_4 on the O_2-activated In-CHA zeolite was monitored using IR spectroscopy where adsorbed formic acid was generated at room temperature. The adsorption and C−H activation of CH_4 on our plausible model of the In-oxo clusters were theoretically investigated using density functional theory calculations. We found that CH_4 is likely to adsorb and react more easily on dinuclear In-oxo ions than on monomeric In-oxo ions and that that the C−H bond cleavage reaction occurs via a heterolytic pathway rather than a homolytic pathway. This study reveals the potential of multinuclear In-oxo clusters as active sites for the transformation of CH_4 to oxygenates under mild reaction conditions.

1. Introduction

Multinuclear metal-oxo clusters, which are composed of a few metal and oxygen atoms, are expected to show unique catalytic differences from isolated metal ions and bulk metal oxides [1–24]. To date, there have been various studies on polyoxometalates stabilized by inorganic/organic ligands [2–8], metal-oxo clusters immobilized on solid supports (bulk metal oxides [9–12], zeolites [13–22], carbon nanotube [23], and metal-organic frameworks [24,25]), and gas-phase clusters vaporized by molecular beam and selected by mass spectroscopy [26,27]. Of these, aluminosilicate zeolite-supported metal-oxo clusters are promising from the viewpoint of precise synthesis, as well as catalytic application, because of their characteristics [28]; for example, the zeolite frameworks are well-defined and usually contain 6- to 12-membered rings consisting of tetrahedral SiO_4 and AlO_4 units linked through oxygen atoms. Paired Al sites are located on the ring, where multiply charged cations can be stabilized by two anionic sites (Si-O-Al). In addition, the high durability and easy handling of zeolites allow their applications in gas and liquid phase reactions. To date, several metal-oxo clusters in zeolites have been developed, making challenging transformations such as the C–H activation of CH_4 and light alkanes possible [13–20]. Cu-oxo clusters have been most extensively studied for CH_4 activation because they mimic the catalytic activity of copper-containing monooxygenase. For example, the oxidation of CH_4 to MeOH occurs on O_2-activated Cu-exchanged ZSM-5, as reported by Groothaert *et al*. [14] and the dinuclear $[Cu(O)Cu]^{2+}$ cluster was identified as the active site [15]. Cu-exchanged mordenite was also active for CH_4 conversion to MeOH, and a similar Cu dimer was proposed by Snyder *et al*. [16]. Subsequently, the groups of Lercher and Hensen identified the trinuclear $[Cu_3O_3]^{2+}$ cluster in mordenite by X-ray absorption fine structure (XAFS) analysis combined with density functional theory (DFT) calculations [17]. $[Fe_2(\mu_2\text{–}OH)_2(OH)_2(H_2O)_2]^{2+}$ dimer [20] and $[Ga_2O_2]^{2+}$ dimer [18,19] in zeolites also have been found to be active for the oxidation [20] or dehydrogenation of light alkanes [18,19] based on a combination of experimental and theoretical studies. Other metal-oxo clusters of transition metal species, such as Ni, Co, Ag, and Au, have been studied experimentally and/or theoretically for CH_4 oxidation [21,22,29] while the study of typical metal-oxo clusters for CH_4 activation have been rarely reported.

Indium (In)-exchanged zeolites have the potential to activate the C–H bond of CH_4. It has been reported that reductive solid-state ion exchange (RSSIE) between In_2O_3 and H-form zeolites under a H_2 atmosphere around 700–800 K affords isolated In^+ cations bound to the lattice oxygen anions [30,31]. Baba *et al*. reported the reaction of CH_4 with ethylene to propane at 673 K using In-exchanged ZSM-5 (In-ZSM-5), in which the isolated In^+ cations with lattice oxygen anions were considered to cleave the C–H bond of CH_4 heterolytically to give methyl cation-like species [32]. In-exchanged zeolites have also been applied to the selective catalytic reduction (SCR) of NO with CH_4 and O_2 by Kikuchi *et al*. [33] and Szegedi *et al*. [34]. Both groups concluded that the CH_4 SCR reaction occurred on the InO^+ sites in zeolites. Recently, Stepanov *et al*. revealed the activation of CH_4 on O_2-activated In-ZSM-5 at 453–573 K through the H/D exchange reaction [35] and transformation into surface species [36], where the isolated InO^+ cation was proposed as an active site. These studies have demonstrated the activation of the C–H bond in CH_4 by In-exchanged zeolites and O_2-activated ones, while the formation of In-oxo clusters for CH_4 activation has not yet been reported.

Based on the above studies, we expect that multinuclear In-oxo clusters would be synthesized using the zeolites with well-defined paired Al sites and that these clusters would exhibit unique ability for CH_4 activation. In this work, the zeolite-supported In-oxo clusters for CH_4 activation under mild reaction conditions are described based on experimental and theoretical studies. To achieve this goal, a CHA zeolite was utilized as a support because its framework is more robust under thermal conditions than other zeolites [37,38]. This is advantageous to retain their paired Al sites without dealumination during RSSIE and O_2 activation. We found that multinuclear In-oxo clusters were formed by O_2 activation of In-exchanged CHA zeolites (InO_X-CHA) using X-ray absorption fine structure (XAFS) measurement. The formation of In-oxo clusters and their detailed structures are discussed on the basis of *ab initio* thermodynamics analysis. The redox properties of the In species during preparation of In-oxo clusters were also studied by temperature programmed reaction (TPR) and *in situ* XAFS measurement. Concerning CH_4 activation, the room temperature oxidation of CH_4 to formic acid on InO_x-CHA is demonstrated using *in situ* Fourier transform (FT)-IR measurements. The adsorption and activation energies for the cleavage of the C–H bond of CH_4 on plausible In-oxo dimers and monomer were theoretically evaluated by DFT calculations.

2. Experimental and theoretical methodology

2.1 Preparation of O_2-activated In-exchanged CHA zeolite (InO_x-CHA)

In-exchanged CHA (In(I)-CHA) was prepared through the impregnation and RSSIE as follows. First, 1.0 g of CHA zeolite (Tosoh, NH_4^+-type, SiO_2/Al_2O_3 = 22.3, NH_4-CHA) was suspended in an aqueous solution containing 0.1 g of $In(NO_3)_3 \bullet nH_2O$ (Kanto Chemical Co.,Inc.). The water was evaporated from the mixture, and the mixture was dried in an oven and calcined at 773 K in air for 1 h, to afford In_2O_3 loaded on the CHA zeolite (denoted In_2O_3/CHA). Next, In_2O_3/CHA was treated with H_2 flow (20 mL min^{-1}) at 773 K for 30 min to promote RSSIE [30,31]. Hereinafter, the obtained In cation-exchanged CHA was denoted as In(I)-CHA. The O_2 activation of In(I)-CHA was conducted under O_2 flow (20 mL min^{-1}) at 773 K for 30 min. The O_2-activated In-exchanged CHA, InO_X-CHA, was obtained as a white powder.

2.2 Characterization

Powder X-ray diffraction (XRD) patterns were recorded on Rigaku Miniflex using Cu Kα radiation. N_2 adsorption measurements were conducted by using an AUTOSOBB 6AG (Yuasa Ionics Co.). The loading amount of In was determined by energy dispersive X-ray fluorescence (EDX) spectrometry (Shimadzu EDX-700HS). H_2- and O_2-TPRs experiments were carried out using a BELCAT (MicrotracBEL). In_2O_3/CHA (approximately 50 mg) was pretreated at 773 K for 1 h under He. For H_2-TPR, In_2O_3/CHA was cooled to 373 K under He, and then the flow was changed to 5% H_2/Ar at a flow rate of 30 mL min^{-1}. For O_2-TPR, the above H_2-treated In_2O_3/CHA was cooled to 313 K under He, and then the flow was changed to 1% O_2/He at a flow rate of 30 mL min^{-1}. The temperature was increased to 773 K at 20 K min^{-1}, after which the temperature was maintained for 40 min. The H_2 consumption was monitored with a thermal conductivity detector. The O_2 consumption and the amount of gas consumed were investigated by a mass spectrometer (BEL Mass, (MicrotracBEL Inc.)). In K-edge XAFS data were collected in quick mode and recorded in transmission mode at the BL-01B1 and BL-14B2 stations attached to the Si(311) monochromator at SPring-8 (JASRI), Japan (Proposal Nos. 2018B1126 and 2018B1568). For *in situ* XAFS measurement, a flow-type cell connected to a flow reaction system was utilized. The X-ray absorption near-edge structure (XANES) and extended XAFS

(EXAFS) analyses were conducted using the REX ver. 2.5 program (Rigaku). The coordination numbers (CN) and interatomic distances (R) were estimated by curve-fitting analysis using In−O and In−In shell parameters obtained from reference samples of In_2O_3. Scanning transmission electron microscopy (STEM) images were taken on a JEM-ARM200F microscope equipped with a JED-2300 EDX spectrometer (JEOL) at an acceleration voltage of 200 kV. The Cs-corrector CESCOR (CEOS) was used in STEM mode.

2.3 Reaction of CH_4 on InO_X-CHA

The IR spectroscopy study of the reaction of CH_4 was conducted with a JASCO FT/IR-4600 spectrometer equipped with a mercury cadmium telluride (MCT) detector using a flow-type IR cell connected to a flow reaction system. The IR disc of In_2O_3/CHA (40 mg, 20 mm) was first dehydrated under N_2 flow at 773 K (90 mL min^{-1}) and then H_2 treatment (20 mL min^{-1}) followed by O_2 treatment (10% balanced with N_2, 100 mL min^{-1}) was conducted at 773 K. After that a background spectrum was obtained under N_2 flow at 303 K (90 mL min^{-1}). Then, CH_4 (10%) was introduced to the sample, and the IR spectra were recorded. For control experiments, In_2O_3 (99.9%) was commercially purchased from Wako Pure Chemical Industries and then used.

2.4 DFT calculations

DFT calculations were carried out under the periodic boundary conditions using the Vienna *Ab initio* Simulation Package (VASP) [39,40]. The generalized gradient approximation by the Perdew–Burke–Ernzerhof (PBE) exchange-correlation functional was adopted [41], and the dispersion-corrected DFT-D3 method was employed to consider the van der Waals interactions. The Kohn–Sham equations were solved with the projector augmented wave (PAW) method. We checked the convergence of total energy of the models with respect to the number of k points where the consideration of the only Γ point was sufficient for Brillouin zone sampling (See Figure S1†). A modest Gaussian smearing of 0.05 eV was applied to the band occupations around the Fermi level, and the total energies were extrapolated to $\sigma \to 0$. The plane-wave cutoff energy was set to 500 eV, and spin−polarization was considered in all calculations. For geometry optimization, the lattice parameters were fixed (a = b =

13.675 Å, *c* = 14.767 Å, α = β = 90.0°, γ = 120° and Si/Al = 17),[42] and the forces on atoms were minimized to be less than 0.03 eV/Å. The climbing image nudged elastic band (CI-NEB) method was used to locate the transition-state structures for the C−H bond cleavage of methane on the In-oxo species. The spring constant between adjacent images was set to 5.0 eV/Å^2, and the quasi-Newton algorithm was adopted for relaxing the geometry in the NEB approach while the cutoff was set to 400 eV due to the high computational cost.

XANES spectra were simulated for the DFT-optimized structures using the FDMNES software [43,44]. For simulating the In foil, a unit cell consisting of two In atoms (*a* = 3.309 Å, *b* = 3.309 Å, *c* = 5.016 Å, and α = β = γ = 90.0°) was used, while the model of In_2O_3 consisting of 32 In atoms in the supercell (*a* = *b* = *c* = 10.299 Å and α = β = γ = 90.0°) was employed to simulate bulk In_2O_3. The simulated spectra were normalized based on the number of In atoms in each system.

Ab initio thermodynamic analysis was used to account for the presence of O_2 and H_2O as well as the effect of the temperature on the catalyst activation [45]. We consider the following equilibrium reaction:

$$x\mathrm{In(OH)/CHA} + (1-x)\mathrm{CHA\_2H} + \frac{(2m-3x-n+2)}{4}\mathrm{O_2} + \frac{(x+n-2)}{2}\mathrm{H_2O} \leftrightharpoons \mathrm{In}_x\mathrm{O}_m\mathrm{H}_n\mathrm{/CHA} \quad (1)$$

The corresponding reaction energy is represented as

$$\Delta E = E_{In_xO_mH_n/CHA} - xE_{In(OH)/CHA} - (1-x)E_{CHA\_2H} - \frac{(2m-3x-n+2)}{4}E_{O_2} - \frac{(x+n-2)}{2}E_{H_2O} \quad (2)$$

where $E_{\mathrm{In}_x\mathrm{O}_mH_n/\mathrm{CHA}}$ is the total energy of the CHA zeolite model containing In-oxo species. $E_{\mathrm{In(OH)/CHA}}$ is the energy of the In-CHA model containing $[In(OH)]^{2+}$ ions to compensate for the negative charge of two Al atoms in the zeolite framework (In/Al = 0.5). E_{CHA_2H}, E_{O_2}, and E_{H_2O} represent the computed energies of the CHA zeolite possessing two H atoms for charge compensation, gaseous water, and oxygen molecules, respectively. The accompanying change in the free energy, ΔΓ, is defined as

$$\Delta\Gamma(T,p) = \frac{1}{A}\left[\Delta E - \frac{(2m-3x-n+2)}{2}\Delta\mu_O - \frac{(x+n-2)}{2}\Delta\mu_{H_2O}\right] \quad (3)$$

where A represents the area of the unit cell. The chemical potential, $\Delta\mu$, are described as

$$\Delta\mu_O(T,p) = \frac{1}{2}\left[\Delta\mu_{O_2}(T,p^0) + RTln\left(\frac{p_{O_2}}{p^0}\right)\right] \quad (4)$$

$$\Delta\mu_{H_2O}(T,p) = \Delta\mu_{H_2O}(T,p^0) + RTln\left(\frac{p_{H_2O}}{p^0}\right) \quad (5)$$

The temperature (*T*) and partial pressure (P_{O2} or P_{H2O}) dependencies of the chemical potentials of O_2/H_2O were calculated from the differences in the enthalpy (*H*) and entropy (*S*) of each molecule with respect to the reference state at 0 K. The values of $H(T, p^0)$, $H(0\text{ K}, p^0)$, $S(T, p^0)$, and $S(0\text{ K}, p^0)$ in thermodynamic tables were used for standard pressure (1 atm) [46].

To discuss the molecular-orbital interactions, DFT calculations using a cluster model were carried out with the Gaussian 16 package [47]. The cluster model was constructed from the optimized structure mentioned above (a .mol file can be found in the ESI†). The hybrid B3LYP functional was used [48–50], and the SDD basis sets and D95** basis sets were applied for the In atoms and the Si, Al, O, and H atoms, respectively. In addition, the vdW-D2 correction was adopted. During geometry optimization, all atoms except for terminating H atoms were allowed to relax. The locations of the terminating H atoms were determined by prior geometry optimization where only the terminating H atoms were relaxed while all other atoms were fixed in the crystalline structure [51]. All optimized structure files are provided in the ESI†.

3. Results and discussion

3.1 Morphologies and colors of the In-exchanged zeolites

To characterize the morphologies of the zeolites, we carried out XRD measurements and N_2 adsorption measurements of In_2O_3/CHA and InO_X-CHA. The XRD patterns of In_2O_3/CHA and InO_X-CHA were similar to that of H-CHA (prepared by calcination of NH_4-CHA at 773 K) (Figure 1(a)), which indicates that the crystal structure of CHA was maintained [52]. The specific surface areas (Table S1 in the ESI†), as determined by the Brunauer–Emmett–Teller (BET) method from N_2 adsorption isotherms (Figure 1(b)), of H-CHA, In_2O_3/CHA, and InO_X-CHA were 833, 785, and 710 $m^2\ g^{-1}$, respectively. The pore volumes of H-CHA, In_2O_3/CHA, and InO_X-CHA were determined as 0.402, 0.378, and 0.344 mL g^{-1}, respectively. These results show that the pore structure of the CHA zeolites did not change during preparation. The smaller specific surface area and pore volume of InO_X-CHA than H-CHA and In_2O_3/CHA are ascribed to encapsulation of In species into zeolites. EDX analysis of In_2O_3/CHA revealed that the In loading amount was 3.2 wt%, which corresponds to In/Al ≈ 0.2. Figure 2 shows photographs of In_2O_3/CHA, In(I)-CHA, and InO_X-CHA. First, after impregnation followed by calcination, In_2O_3/CHA was a pale-yellow color (Figure 2(a)). During H_2 reduction of In_2O_3/CHA, the color changed from pale-yellow to white (Figure 2(b)), indicating the absence of aggregated In(0) metal species in In(I)-CHA. After the O_2 treatment of In(I)-CHA, the white color of the catalyst was maintained but differed from that of In_2O_3/CHA (Figure 2(c)), suggesting the formation of In-oxo species unlike In_2O_3.

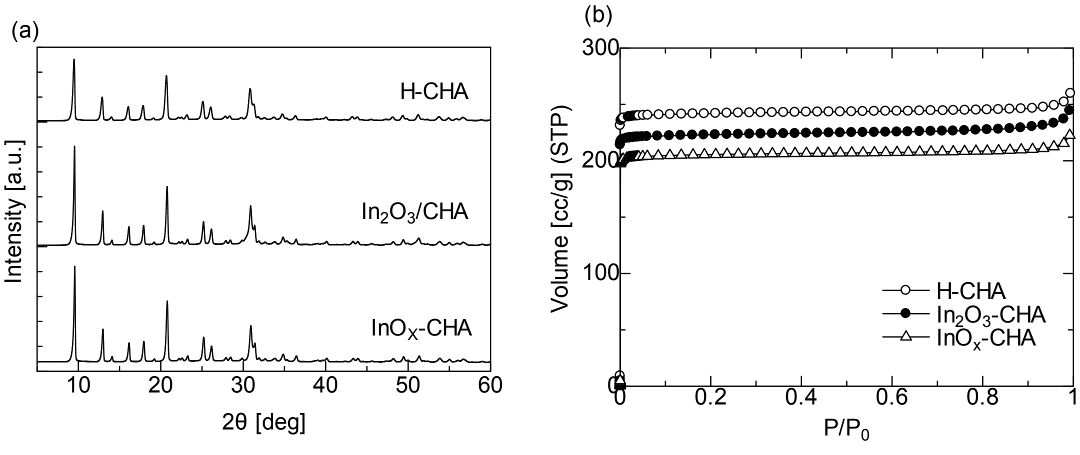

Figure 1. (a) XRD patterns and (b) N_2 adsorption isotherms of H-CHA, In_2O_3/CHA, and InO_X-CHA.

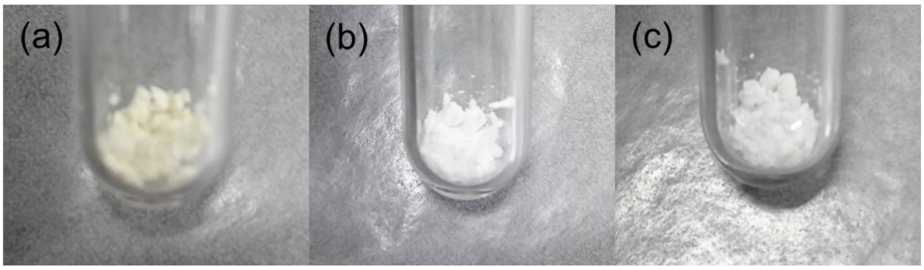

Figure 2. Photographs of (a) In_2O_3/CHA, (b) In(I)-CHA, and (c) InO_X-CHA.

3.2 STEM observation

The formation of highly dispersed In species was supported by STEM observation. The annular bright field and high-angle annular dark-field STEM (ABF- and HAADF-STEM, respectively) images of In_2O_3/CHA show that many aggregated In_2O_3 species (about 10–30 nm) were present on the CHA zeolite (Figure 3). In contrast, the aggregated species was scarcely observed in the STEM images of InO_X-CHA (Figures 4(a) and (b)). The distribution of In species was also determined by HAADF-STEM with EDX elemental mapping. The elemental mapping of InO_X-CHA clearly shows the high dispersion of In species in the CHA zeolite (Figure 4). Note that aggregated In species formed during STEM observation (Figure 5). This result indicates that highly dispersed In species in the zeolite framework can easily be aggregated by the electron beam, making STEM observation difficult [53].

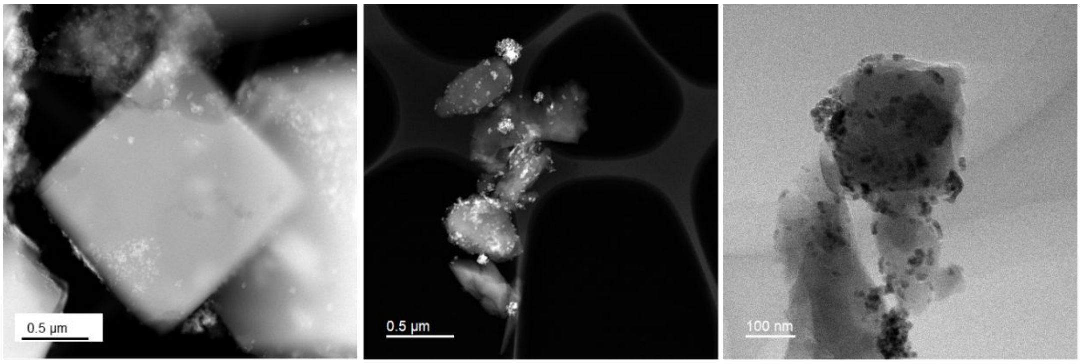

Figure 3. ABF- and HAADF-STEM images of In_2O_3/CHA.

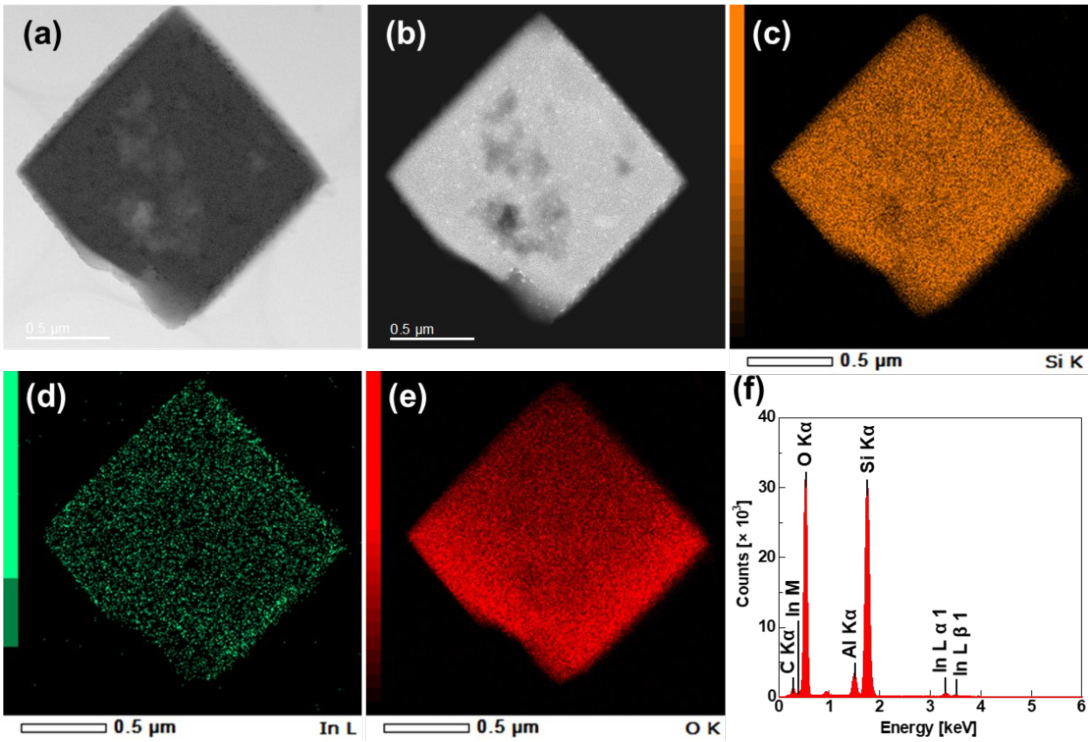

Figure 4. (a) ABF- and (b) HAADF-STEM images of InO_X-CHA. Elemental mapping images of (c) Si, (d) In, and (e) O, and (f) EDX spectrum.

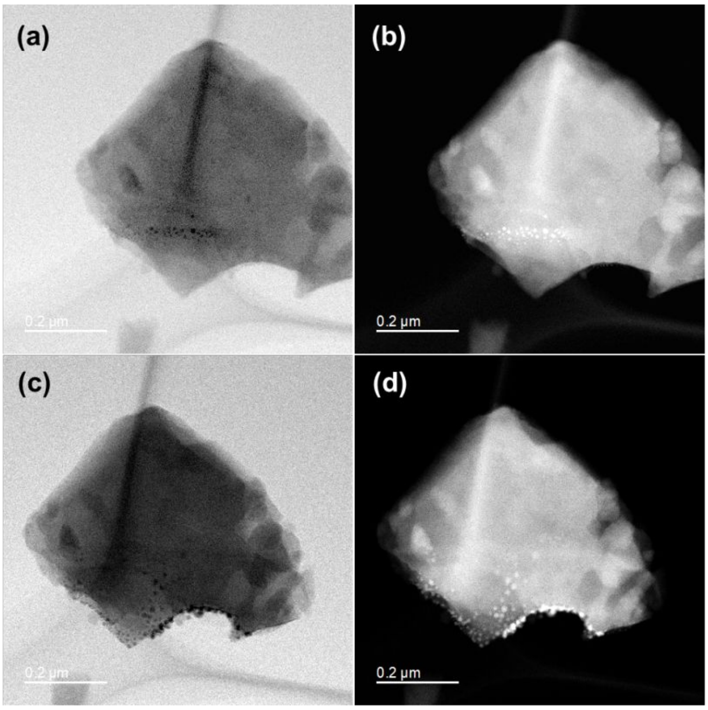

Figure 5. Aggregation of In species during STEM observation. (a) ABF- and (b) HAADF-STEM images of InO_X-CHA. The lower two images ((c) and (d)) were measured 12 min after collecting the upper two images.

3.3 H_2- and O_2-TPR measurements

The reduction profile of the In species in In_2O_3/CHA was investigated using H_2-TPR measurements. Figure 6(a) shows the H_2-TPR profiles. The reduction peak was observed around 573–773 K and the amount of H_2 consumed was determined to be 18 µmol. This value is similar to the amount of In species in In_2O_3/CHA used for H_2-TPR (In: 15 µmol). Lónyi *et al*. reported that the H_2-TPR profile during RSSIE between In_2O_3 and H-mordenite showed a reduction peak around 623–773 K. They also found that the molar ratio of the consumed H_2 and the In species are almost same [31]. Accordingly, the reduction peak observed after the H_2 treatment of In_2O_3/CHA corresponds to the occurrence of the RSSIE between In(I) ions and protons in CHA zeolite. The oxidation of In(I)-CHA was also carried out by O_2-TPR. The O_2-TPR profile (Figure 6(c)) showed a peak corresponding to the oxidation of reduced In species. Furthermore, H_2-TPR measurement was examined for InO_X-CHA where the position of reduction peak shifted toward lower temperature (473–723 K) from that in the case of In_2O_3/CHA (Figure 6(a) vs 6(b)). These observations suggest the formation of highly dispersed In-oxo species unlike In_2O_3, which is consistent with the results of the STEM observations.

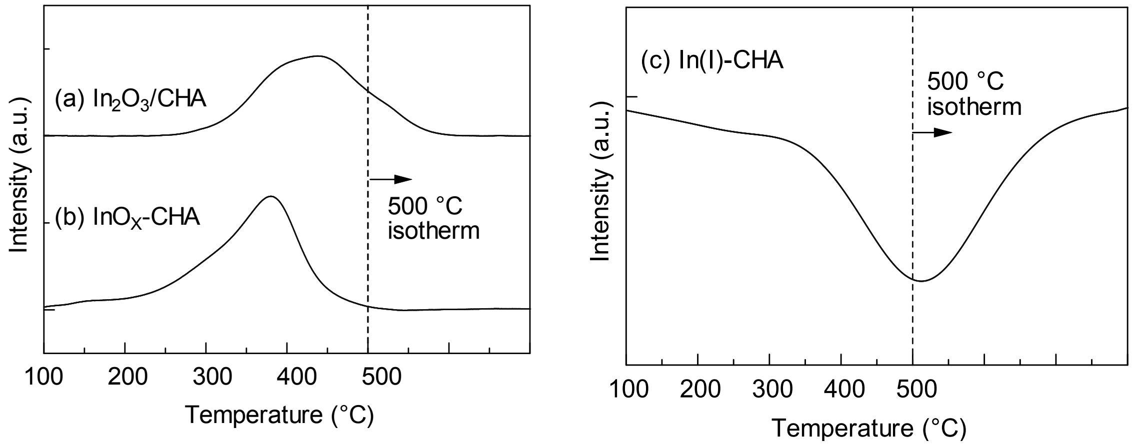

Figure 6. H_2-TPR profiles of (a) In_2O_3/CHA and (b) InO_X-CHA. (c) O_2-TPR profile of In(I)-CHA.

3.4 XAFS measurements

To obtain insight into the In species in the In-exchanged CHA zeolites, *in situ* XAFS measurements were carried out. The normalized XANES spectra and Fourier transforms (FT) of the k^3-weighted EXAFS spectra are summarized in Figures 7(a) and 7(c), respectively. First, the edge position of

In_2O_3/CHA (E_0 = 27935.9 eV) was almost the same as that of In_2O_3 powder (E_0 = 27935.4 eV) and different from that of In foil (E_0 = 27932.6 eV). The FT of EXAFS spectrum of In_2O_3/CHA showed three peaks, which were also observed in that of In_2O_3 powder (Figure 7(c)). The first peak can be attributed to the In–O shell, and the second and third peaks are assignable to two-types of In–In shells, respectively. These results are evidence for the existence of In_2O_3 species in In_2O_3/CHA.

After H_2 treatment (5% balance with He) of In_2O_3/CHA at 773 K, the absorption edge shifted to a lower energy (E_0 = 27931.7 eV). Figure 7(b) shows the XANES spectra during H_2 treatment in which three isobestic points were observed; these are marked with vertical dotted lines. These edge shift and isobestic points are similar to the observations made for the XANES spectra of Ga-exchanged zeolites during H_2 treatment in a previous paper [54], where the type of Ga species (isolated Ga^+ cation or Ga-hydride species) is controversial. Hock *et al.* claimed that the edge shift can be interpreted as evidence of Ga-hydride species on the basis of a comparison of XANES spectra with organometallic model compounds [55]. In contrast, Lercher *et al.* concluded that Ga^+ cation was selectively formed based on the H_2-TPR measurement [56]. Considering the RSSIE between In_2O_3 and H-zeolites reported in previous papers [30,31], the energy shift in In K-edge XANES spectra can be ascribed to the reduction of In^{3+} species (In_2O_3) to In^+ cations. However, the simulated XANES spectra suggested the formation of In-hydride (In^+-H^-) species [57–59] rather than In^+ cations (Figure S2†). The speciation of In after RSSIE is currently under study using other spectroscopic and theoretical methods.

After an He purge followed by O_2 treatment (5% balance with He) of In(I)-CHA at 773 K, the absorption edge returned to a similar value to that of In_2O_3 (E_0 = 27934.7 eV), indicating that In^+ ions were oxidized to In^{3+} species (Figure 7(a)). In the FT of the EXAFS spectrum of InO_X-CHA (Figure 7(c)), the two peaks assignable to In–O and In–In shells were observed, which is different from the cases of In_2O_3 and In_2O_3/CHA. The curve fitting analysis indicated that the CNs are 4.9 and 2.3, respectively (Table 1). From the results obtained from XAFS measurements, multinuclear In-oxo clusters were generated in the CHA zeolites. Thus, in conclusion, the In_2O_3 loaded on H-CHA was reduced by H_2 treatment to afford isolated In^+ ions in the CHA zeolite through RSSIE and, then, the dispersed In^+ ions reacted with O_2, resulting in the formation of In-oxo clusters.

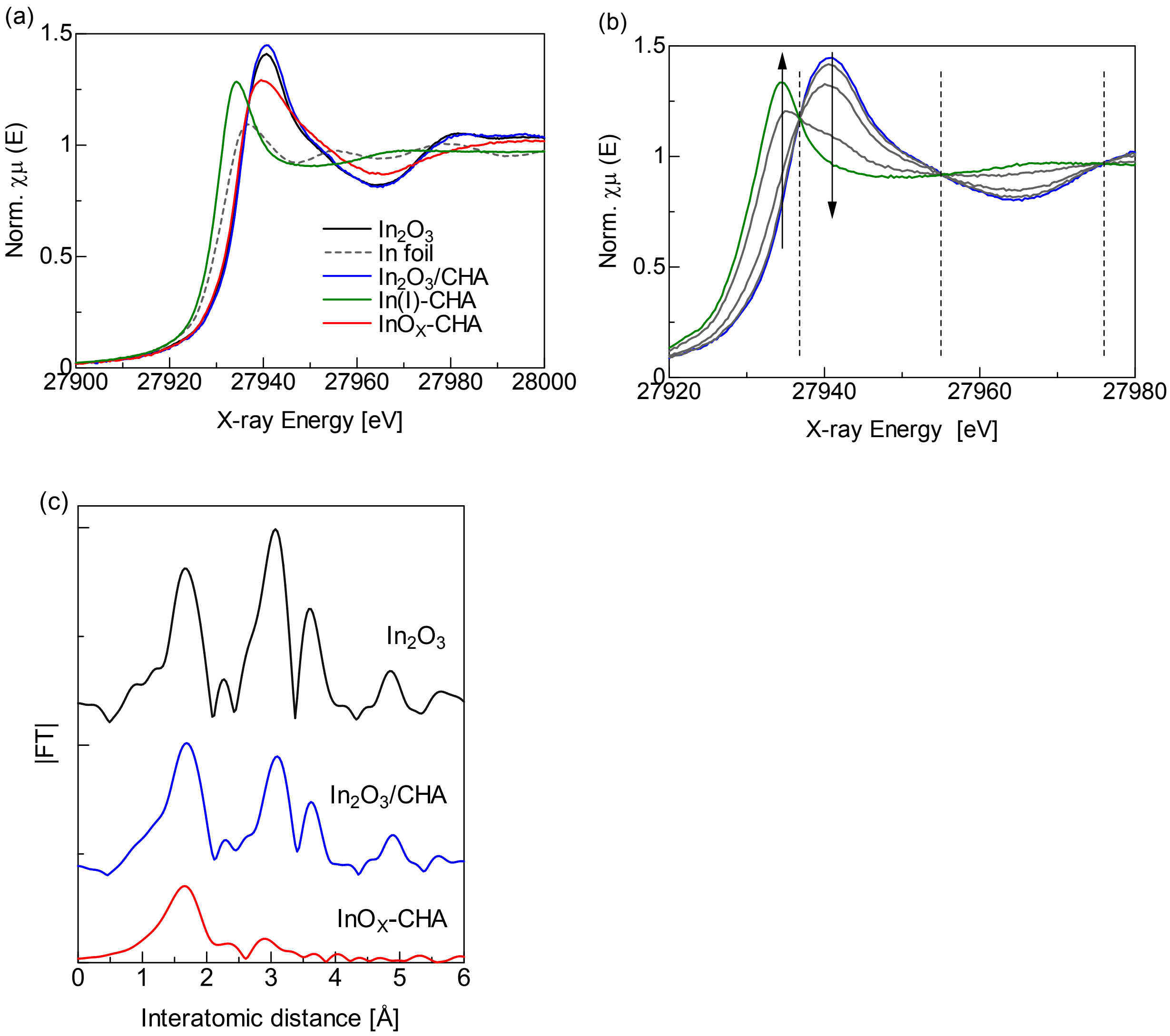

Figure 7. (a) Normalized In K-edge XANES spectra of In_2O_3, In foil, In_2O_3/CHA, In-CHA (after H_2 treatment of In_2O_3/CHA), InO_X-CHA (after O_2 treatment of In_2O_3/CHA). (b) *In situ* In K-edge XANES spectra during H_2 treatment of In_2O_3/CHA. Dotted lines show isosbestic points. (c) FT of k^3-weighted EXAFS oscillations measured at room temperature for of In_2O_3, In_2O_3/CHA, and InO_X-CHA.

Table 1. Curve-Fitting Analysis of In K-Edge EXAFS of InO_X-CHA

Sample	Shell	CN[a]	R (Å)[b]	ΔE (eV)[c]	σ (Å)[d]	*R* (%)[e]
InO_X-CHA	In–O	4.95 ± 1.04	2.12 ± 0.02	-0.122	0.086	3.19
	In–In	2.38 ± 1.58	3.25 ± 0.03	-2.648	0.098	
In_2O_3 (reference)	In–O	6[f]	2.19[f]	-	-	-
	In–In	6[f]	3.34[f]	-	-	-

a Coordination numbers. b Bond distance. c Increase of the threshold energy. d Debye−Waller factor. e Residual factor. f Obtained from crystallographic data.

3.5 *Ab initio* thermodynamic analysis

We employed an *ab initio* thermodynamic approach [60] to predict the structures of the In-oxo clusters in InO_X-CHA. This approach has been utilized for predicting the structures of the key multinuclear metal-oxo clusters of Cu, Fe, and Al cations in zeolites [17,45,61–64]. Three types of paired Al sites were examined as coordination sites of the In-oxo clusters. The first type possesses two Al sites that are separated by three Si centers in an eight-membered ring (8MR) and has a connectivity distance of three, denoted as the forth-nearest-neighbor site, 8MR(4NN). The other two are represented as 8MR(3NN) and 6MR(3NN) (Figure 8). Our computational data set includes one monomer, two dimers, one trimer and three tetramers. Details of models are provided in the ESI†. To reflect the reaction conditions of the O_2 treatment of In(I)-CHA, we have shown the computational free energies for the formation of In-oxo ions (Figures 9(a)–(c)) and the phase diagram representing the lowest-energy species (Figures 9(d)–(f)) at 800 K as a function of O_2 and H_2O chemical potentials ($\Delta\mu_{O2}$ and $\Delta\mu_{H2O}$, respectively). $\Delta\mu_{O2}$ and $\Delta\mu_{H2O}$ are translated into partial pressure scales (P_{O2} and P_{H2O}, respectively) at 800 K in the phase diagram.

In the phase diagram for the 8MR(4NN) site (Figure 9(d)), the equilibrium In-oxo structure is sensitive to the value of $\log(P_{H2O})$, and the $[In_2O_2]^{2+}$ ion (yellow) is the lowest-energy In-oxo ion at the lowest H_2O partial pressure. As $\log(P_{H2O})$ increases, the $[In_2O_2]^{2+}$ ion changes to a tetrameric structures, such as $[In_4O_4]^{2+}$ (gray) and $[In_4O_4(OH)_2]^{2+}$ ions (green), and $[In_2(OH)_4]^{2+}$ ion (blue) is the lowest-energy In-oxo ion at high H_2O partial pressures. At a $\log(P_{O2})$ of around -1 or 0 and a low H_2O partial pressure, corresponding to 10% or 100% O_2 flow in dry conditions, the free energy for the formation of the $[In(OH)]^{2+}$ ion is only slightly higher than that of $[In_2O_2]^{2+}$ ion, whereas those of other In-oxo ions are much higher, as shown in Figure 9(a). These results indicate that the $[In_2O_2]^{2+}$ ion is a candidate In-oxo cluster on 8MR(4NN) sites under O_2 condition. Concerning the 8MR(3NN) site, although $[In(OH)]^{2+}$ ion (red) is the lowest-energy In-oxo ion at low H_2O pressures (Figure 9(e)), the free energy for the formation of the $[In_2O_2]^{2+}$ ion is close to that of the $[In(OH)]^{2+}$ ion and much lower than those of the other In-oxo ions (Figure 9(b)), indicating that the $[In_2O_2]^{2+}$ ion is a plausible In-oxo structure for the 8MR(3NN) site. In contrast, for the 6MR(3NN) site, the $[In(OH)]^{2+}$ ion is the most stable structure under all O_2 and H_2O partial pressures (Figures 9(c) and 9(f)). From the phase diagrams, we suggest that multinuclear In-oxo clusters are formed at paired Al sites on 8MR, and the $[In_2O_2]^{2+}$ ion is the most plausible structure among the considered multinuclear clusters. Hereinafter, we consider $[In_2O_2]^{2+}$ on 8MR(4NN) and 8MR(3NN) and $[In(OH)]^{2+}$ on 6MR(3NN) as model dimeric and monomeric In-oxo ions for further discussion.

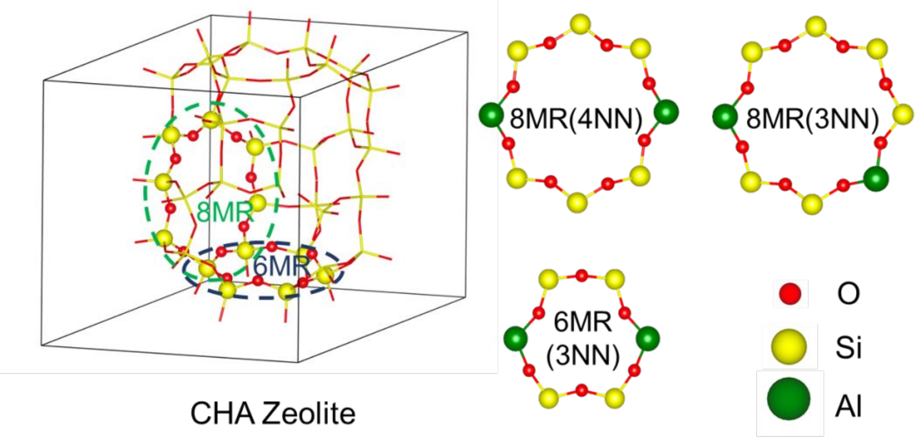

Figure 8. CHA unit cell and Al configurations investigated in periodic DFT calculations. Ovals highlight the locations of 8MR and 6MR.

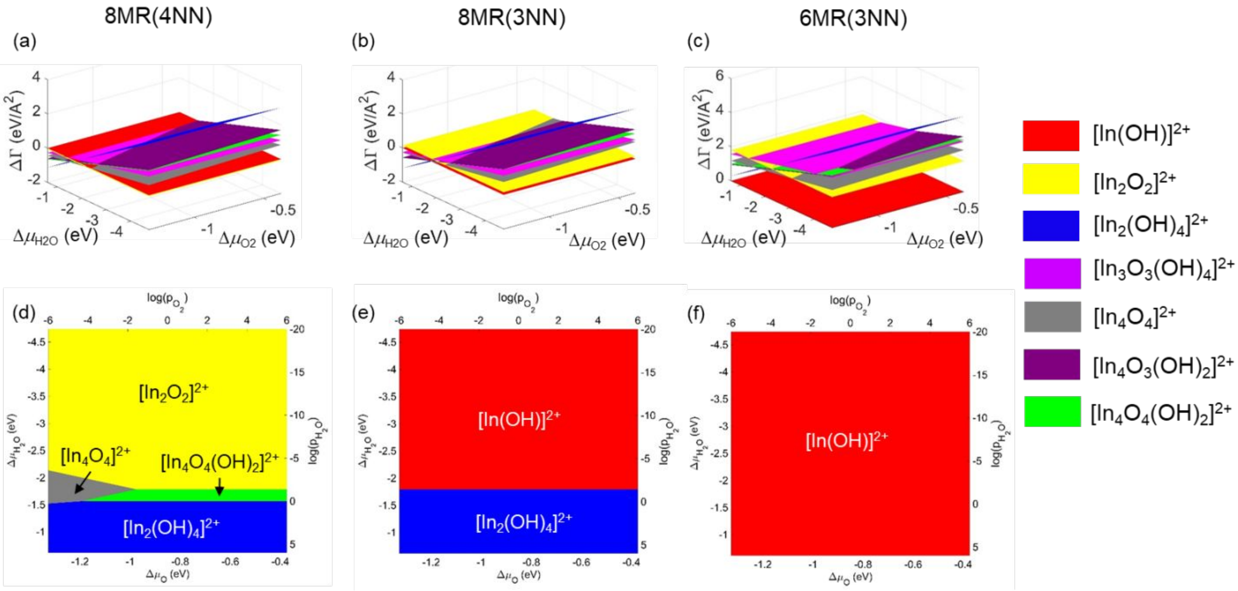

Figure 9. Free energy (ΔΓ) for the formation of the In-oxo ions in CHA (top) and phase diagram showing the lowest-energy In-oxo ions (bottom) as a function of O_2 and H_2O chemical potentials ($\Delta\mu_{O2}$ and $\Delta\mu_{H2O}$, respectively) on (a,d) 8MR(4NN), (b,e) 8MR(3NN), and (c,f) 6MR(3NN).

The optimized structures for $[In_2O_2]^{2+}$ at 8MR(4NN) and 8MR(3NN) sites (denoted as $[In_2O_2]^{2+}$-8MR(4NN) and $[In_2O_2]^{2+}$-8MR(3NN)) and for $[In(OH)]^{2+}$ at 6MR(3NN) ($[In(OH)]^{2+}$-6MR(3NN)) are shown in Figure 10. The In–In distances for $[In_2O_2]^{2+}$-8MR(4NN) is 2.92 Å, which is very similar to that in $[In_2O_2]^{2+}$-8MR(3NN) (2.91 Å), despite the obvious difference in the Al–Al distances (7.88 and 7.23 Å for $[In_2O_2]^{2+}$-8MR(4NN) and $[In_2O_2]^{2+}$-8MR(3NN), respectively). The In–O distances range from 2.07 to 2.10 Å for both $[In_2O_2]^{2+}$ ions. These In–In and In–O distances are different from the case of $[Ga_2O_2]^{2+}$ ions in zeolites reported by Hensen *et al*. [19] where the Ga–Ga and Ga–O distances were calculated to be about 2.49–2.59 and 1.84–1.89 Å, respectively. The In–O–In angles for $[In_2O_2]^{2+}$-8MR(4NN) and $[In_2O_2]^{2+}$-8MR(3NN) are about 88–89°. This value is slightly larger than the Ga–O–Ga angle in $[Ga_2O_2]^{2+}$ ions (about 84–88°). For $[In(OH)]^{2+}$-6MR(3NN), the In–O distance of $[In(OH)]^{2+}$ is 2.02 Å and the Al–Al distance is 5.88 Å. The shorter Al–Al distance in 6MR(3NN) compared to those in 8MR(4NN) and 8MR(4NN) might be one of the reasons why monomeric $[In(OH)]^{2+}$ ions are more stable among the other In-oxo ions. As demonstrated above, $[In_2O_2]^{2+}$ ions are expected to be the most stable In-oxo ions on paired Al sites in 8MR.

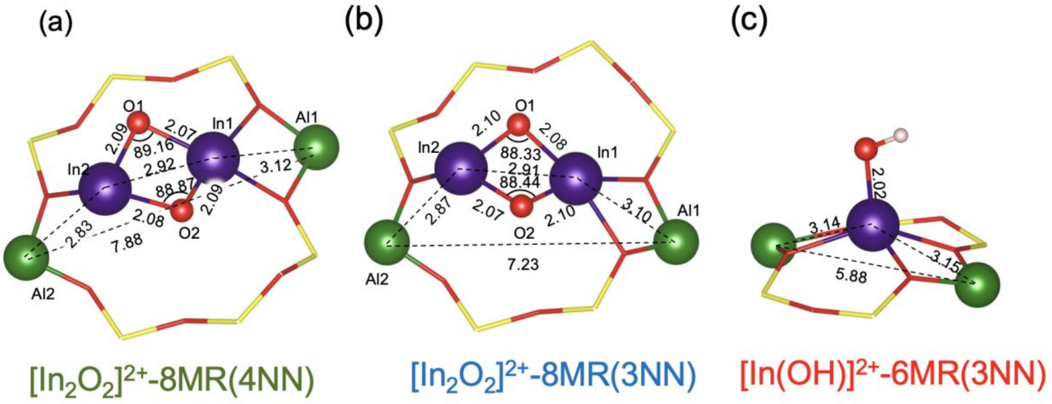

Figure 10. Optimized structures of (a) $[In_2O_2]^{2+}$-8MR(4NN), (b) $[In_2O_2]^{2+}$-8MR(3NN), and (c) $[In(OH)_2]^{2+}$-6MR(3NN).

3.6 Experimental and theoretical investigation for activation of CH_4 on In-oxo clusters

The development of effective catalysts for CH_4 activation under mild conditions is challenging because of the high stability of C–H bonds in CH_4, and various experimental and theoretical studies in this research area have been carried out [29,65–83]. To explore the ability to activate CH_4 of In-oxo clusters supported in CHA, the adsorbed species generated during the reaction of CH_4 on InO_X-CHA at room temperature were studied by *in situ* IR measurements (Figure 11). The FT-IR spectrum contains a peak at 1379 cm^{-1} and a band around 1700 cm^{-1} after 10% CH_4 purge for 100 min followed by an N_2 purge. The first peak can be assigned to C–H bending of adsorbed formic acid [84], and the latter peak was deconvoluted into two peaks at 1710 and 1630 cm^{-1}, which can be attributed to the C=O stretching of adsorbed formic acid and water [84], respectively. The formation of formic acid was supported by the FT-IR measurement after adsorption of formic acid on H-CHA where similar two peaks were observed (Figure S3 in the ESI†). The CH_4-TPR of InO_x-CHA revealed that neither CO_2 nor CO was detected at room temperature, indicating the occurrence of selective oxidation of CH_4 to formic acid. We tried to extract the adsorbed formic acid using D_2O for determination by ^1H NMR measurement according to the previous paper [85], but any peak was not observed in the NMR spectrum, which might be due to difficulty in extraction from the small pore of CHA zeolites. In the control experiments using In_2O_3/CHA and In_2O_3 instead of InO_X-CHA, the spectra did not contain these peaks. The above results show that CH_4 was oxidized to formic acid at room temperature over the In-oxo clusters.

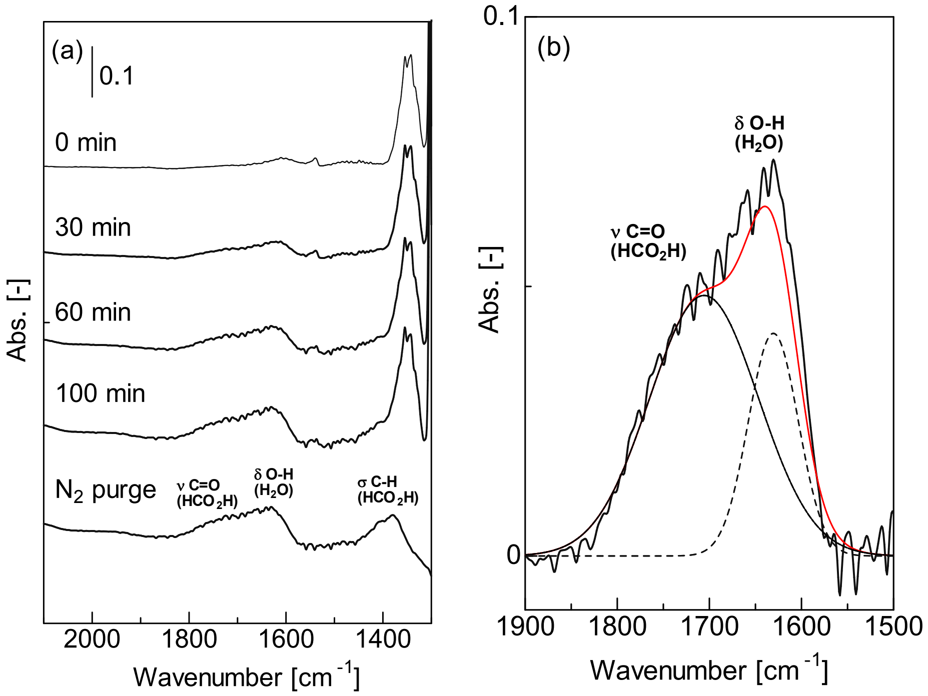

Figure 11. (a) FT-IR spectra during the reaction of CH_4 on InO_X-CHA at room temperature. (b) Curve-fitting of the band around 1800–1600 cm^{-1} in the IR spectrum after N_2 purge.

The C−H bond cleavage is generally regarded as the rate-determining step in the reactions of CH_4

on most heterogeneous catalysts [74], and much effort has been devoted to the study of activation of C−H bond of CH_4 through experimental and theoretical approaches [76,79,80,82,86]. We also investigated the reactivities of the possible In-oxo ions, $[In_2O_2]^{2+}$-8MR(4NN), $[In_2O_2]^{2+}$-8MR(3NN), and $[In(OH)]^{2+}$-6MR(3NN), for the C−H bond cleavage of CH_4 using DFT calculations, and the reaction energy diagrams and geometrical parameters are shown in Figure 12 and Table 2, respectively. The adsorption energies of CH_4 on $[In_2O_2]^{2+}$-8MR(4NN) and $[In_2O_2]^{2+}$-8MR(3NN) are similar (E_{ads} = -43.7 and -41.8 kJ/mol, respectively) and larger than that on $[In(OH)]^{2+}$-6MR(3NN) (E_{ads} = -18.9 kJ/mol). As shown in Figure 12 and Table 2, the shortest In−C distances for $[In_2O_2]^{2+}$-8MR(4NN), $[In_2O_2]^{2+}$-8MR(3NN), and $[In(OH)]^{2+}$-6MR(3NN) are 2.91, 2.87, and 5.36 Å, respectively. In contrast, the four C−H bond distances of the CH_4 molecules adsorbed on each In-oxo ions are almost the same, and the average distance is about 1.10 Å. The H−C−H angles directed toward the In cation of $[In_2O_2]^{2+}$-8MR(4NN) and $[In_2O_2]^{2+}$-8MR(3NN) are 114.3° and 112.4°, respectively. These values are larger than the H−C−H angle of isolated CH_4 (109.7°). These results suggest that CH_4 adsorbs on $[In_2O_2]^{2+}$ ions in an η^2-like fashion, which results in a distorted CH_4 structure. Similar M−H and C−H bond distances and H−C−H angles were reported by Kuroda *et al.* in their theoretical studies of CH_4 activation by Zn and Mg cations in zeolites [87]. In contrast, the H−C−H angle for $[In(OH)]^{2+}$-6MR(3NN) (109.0°) is very close to that in isolated CH_4.

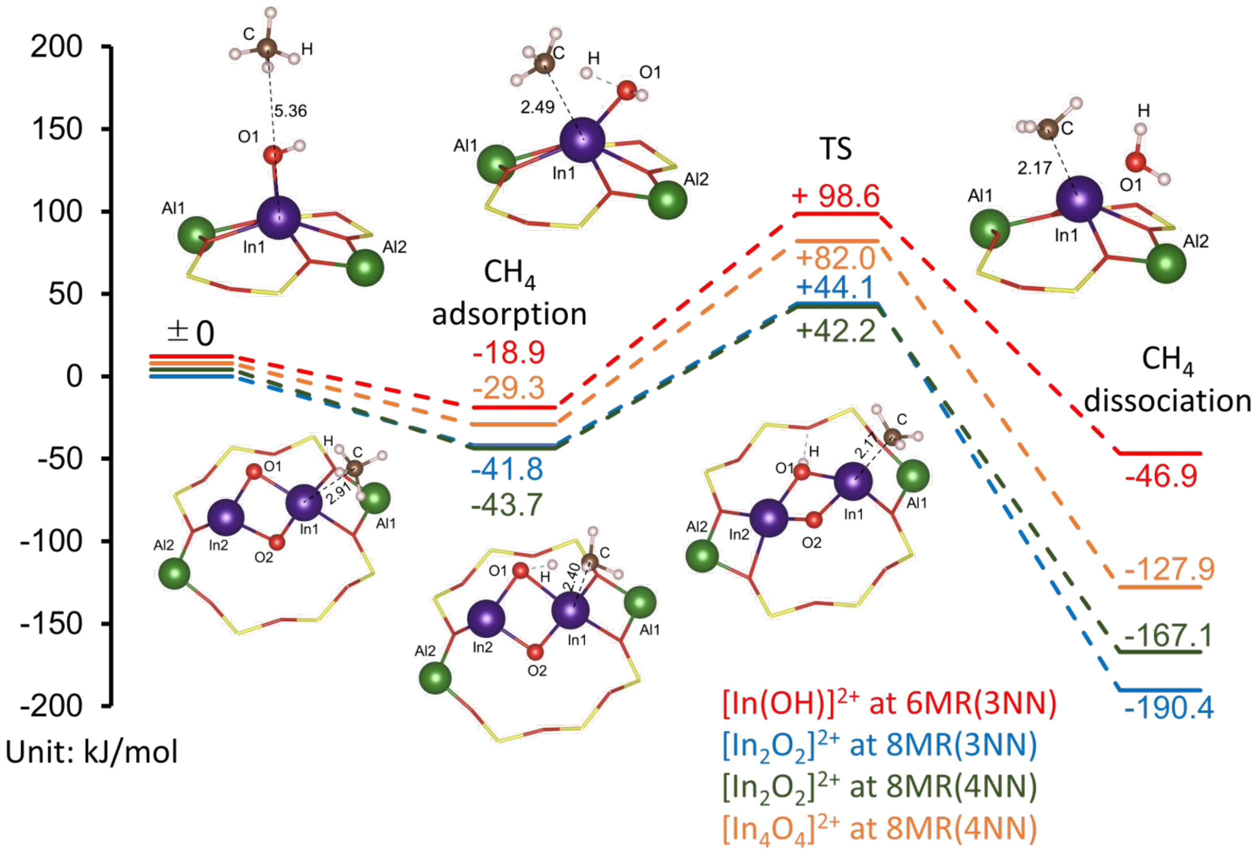

Figure 12. Reaction energy diagrams of the intermediates and transition states for the activation of CH_4 by $[In_2O_2]^{2+}$-8MR(4NN) (green), $[In_2O_2]^{2+}$-8MR(3NN) (blue), $[In(OH)_2]^{2+}$-6MR(3NN) (red), and $[In_4O_4]^{2+}$-8MR(4NN) (orange). Optimized structures of the intermediates and transition states for $[In_2O_2]^{2+}$- 8MR(4NN) (bottom) and $[In(OH)]^{2+}$-6MR(3NN) (top) are included in the figure.

Table 2. Geometrical parameters (distances in Å and bond angles in degrees) for adsorption (Ads), transition-state (TS), dissociation (Dis) structures of $[In_2O_2]^{2+}$-8MR(4NN), $[In_2O_2]^{2+}$-8MR(3NN), $[In(OH)]^{2+}$-6MR(3NN), and $[In_4O_4]^{2+}$-8MR(4NN).

	$[In_2O_2]^{2+}$-8MR(4NN)			$[In_2O_2]^{2+}$-8MR(3NN)			$[In(OH)]^{2+}$-6MR(3NN)			$[In_4O_4]^{2+}$-8MR(4NN)		
	Ads	TS	Dis	Ads	TS	Dis	Ads	TS	Dis	Ads	TS	Dis
In1–In2	2.94	3.04	3.17	2.92	3.03	3.15	-	-	-	3.18	3.28	3.47
In1–O1–In2	89.3	88.6	94.2	88.6	88.6	92.9	-	-	-	92.9	88.0	81.8
In1–O2–In2	89.9	94.8	100.3	88.7	94.1	99.9	-	-	-	92.4	93.4	101.7
C–H	1.10	1.38	-	1.11	1.37	-	1.10	1.35	-	1.10	1.33	-
O1–H	3.39	1.34	0.98	3.98	1.36	0.98	2.65	1.29	-	3.10	1.37	0.97
O1–C	4.09	2.70	3.90	4.37	2.70	3.98	3.35	2.61	3.13	3.45	2.68	3.27
In1–O1	2.10	2.26	2.18	2.08	2.24	2.22	-	-	-	2.19	2.21	2.30

In1–O2	2.09	2.06	2.11	2.11	2.08	2.11	-	-	-	2.20	2.11	2.13
In1–C	2.91	2.40	2.17	2.87	2.40	2.17	5.36	2.49	2.17	3.81	2.46	2.16
H1–C–H2	114.3	-	-	112.4	-	-	109.7	-	-	109.7	-	-

Following adsorption, CH_4 is activated by the weakening of the C–H bond via a transition state (TS). The C–H bond distances in the TS for $[In_2O_2]^{2+}$-8MR(4NN), $[In_2O_2]^{2+}$-8MR(3NN), and $[In(OH)]^{2+}$-6MR(3NN) are almost the same (1.38, 1.37, and 1.35 Å, respectively), whereas the activation energies for $[In_2O_2]^{2+}$-8MR(4NN) and $[In_2O_2]^{2+}$-8MR(3NN) are much lower than that for $[In(OH)]^{2+}$-6MR(3NN) (E_a = 85.9 and 85.9 vs 117.5 kJ/mol, respectively). After the dissociation of the C–H bond, an O–H bond is formed at the bridging O atom, and the resulting CH_3 group forms an In–CH_3 fragment for $[In_2O_2]^{2+}$-8MR(4NN) and $[In_2O_2]^{2+}$-8MR(3NN). In the case of $[In(OH)]^{2+}$-6MR(3NN), water is formed from the OH group, accompanied by the formation of an In–CH_3 bond [88]. All the In–C distances are 2.17 Å, which is very similar to that in the $In(CH_3)_3$ model calculated by Gueorguiev *et al.* [89]. The reactions of the C–H bond cleavage for $[In_2O_2]^{2+}$-8MR(4NN) and $[In_2O_2]^{2+}$-8MR(3NN) are more exothermic (ΔE = 123.4 and 148.6 kJ/mol) than that of $[In(OH)]^{2+}$-6MR(3NN) (28.0 kJ/mol). These results suggest that CH_4 is likely to adsorb and react more easily on the $[In_2O_2]^{2+}$ ions rather than $[In(OH)]^{2+}$ ions.

Furthermore, the reactivity of a possible higher oligomer, $[In_4O_4]^{2+}$-8MR(4NN) (the optimized structure is shown in Figure S4†), was investigated by DFT calculation and compared with $[In_2O_2]^{2+}$-8MR(4NN) and $[In(OH)]^{2+}$-6MR(3NN) as dimeric and monomeric In-oxo ions, respectively. The C–H bond cleavage over $[In_4O_4]^{2+}$-8MR(4NN) is exothermic (ΔE = 98.6 kJ/mol) and affords an O–H bond and an In–CH_3 fragment as is the case for $[In_2O_2]^{2+}$-8MR(4NN) (Figure 12). The adsorption energy of CH_4 on $[In_4O_4]^{2+}$-8MR(4NN) is -29.3 kJ/mol, which is moderate among the monomeric, dimeric and tetrameric In-oxo ions explored in this study. The calculated activation energy for $[In_4O_4]^{2+}$-8MR(4NN) is much higher than that for $[In_2O_2]^{2+}$-8MR(4NN) (E_a = 111.4 vs 85.9 kJ/mol, respectively) and lower than that for $[In(OH)]^{2+}$-6MR(3NN) (117.5 kJ/mol). This comparison based on DFT calculation showed that dimeric In-oxo clusters are more reactive than tetrameric ones. We also calculated the partial charge (q) of O and In atoms (q(O) and q(In), respectively) to investigate the correlation between of E_a and q(O)/q(In) for four In-oxo ions. The plots in Figure 13 show that E_a decreases linearly with a decrease of q(O) (Figure 13(a)) while no obvious correlation is found between E_a and q(In) (Figure 13(b)). The similar q(O) dependency of the activation energy was observed in DFT calculation for C−H activation on bimetallic Co−M oxide clusters reported by Gagliardi et al. [90]. These results showed that the difference of reactivity among monomeric, dimeric, and tetrameric In-oxo ions is ascribed to the difference of nature of bridging O atom, demonstrating the potential of partial charge of bridging O atom as a useful descriptor to rationalize and predict the reactivity of metal-oxo clusters.

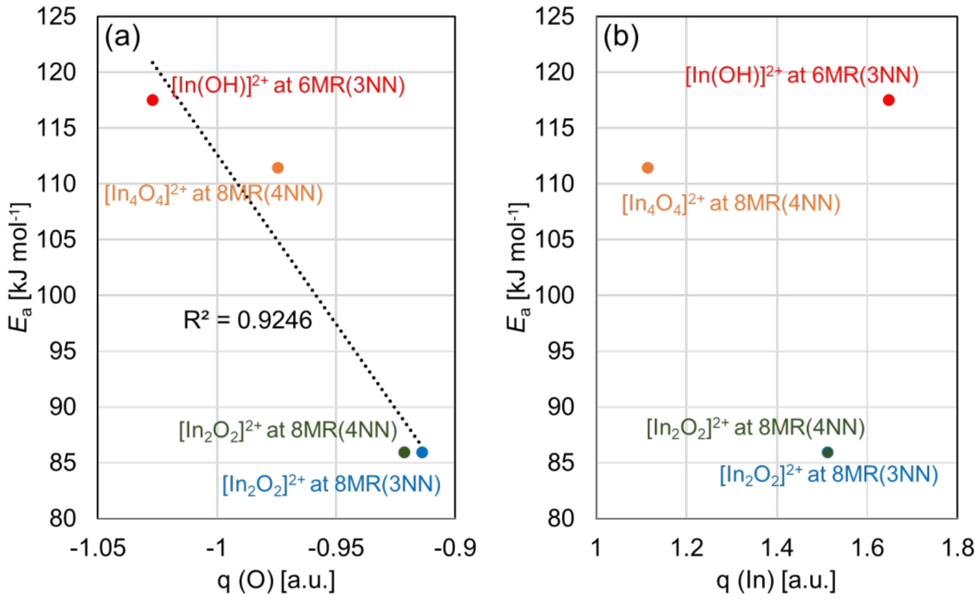

Figure 13. Plots of the C−H activation energy (E_a) against partial charge of (a) bridging O atom and (b) In. For (a), linear regression line y = -304.06x - 191.45, R² = 0.9246.

To gain some insight into the adsorption and activation mechanisms of CH_4 on $[In_2O_2]^{2+}$-8MR(4NN), we analyzed the molecular orbitals. It is considered that there are two main interactions between the adsorbates and active metal centers: A) charge transfer interactions from the occupied orbital of the adsorbate to an empty orbital of the metal center and B) charge transfer interactions from the occupied orbital of the metal center to the empty orbital of the adsorbate [86,91]. The energy gap between the lowest occupied molecular orbital (LUMO) of $[In_2O_2]^{2+}$-8MR(4NN) and the highest occupied molecular orbital (HOMO) of CH_4 is 8.36 eV, which is smaller than that between the HOMO of $[In_2O_2]^{2+}$-

8MR(4NN) and the LUMO of CH_4 (10.26 eV) (Figure 14(a)), indicating that the charge transfer from the HOMO of CH_4 to the LUMO of $[In_2O_2]^{2+}$-8MR(4NN) is more likely to occur. As shown in Figure 14(a), the LUMO of $[In_2O_2]^{2+}$-8MR(3NN) is localized at the In1 cation where CH_4 interacts as indicated in the optimized structures (Figure 12). The charge density difference for CH_4 adsorption on $[In_2O_2]^{2+}$-8MR(4NN) (Figure 14(b)) shows the main transfer of electron density from the C–H bonds to the region between the C–H bond and the In1 cation, indicating the heterolytic cleavage of the C–H bond [87,92,93]. Heterolytic cleavage is supported by a comparison of the energy diagrams (Figure S5†), which show that the activation energy for the radical intermediate is significantly larger (298.3 kJ/mol) than that for heterolytic cleavage (85.9 kJ/mol, Figure 12) [92]. It is well-known that the activation of CH_4 and other light alkanes over transition metal surfaces and multinuclear Cu-oxo and Fe-oxo clusters is initiated by the homolytic cleavage of C–H bonds to give radical intermediates [15,17,20,51,77,82,83]. Although there are some reports suggesting the heterolytic cleavage of C–H bonds of those substrates by using Zn or Ga ion-exchanged zeolite materials [87,92,93], the present In-CHA system still serves as a rare example that can activate CH_4 through the heterolytic cleavage of the C–H bond.

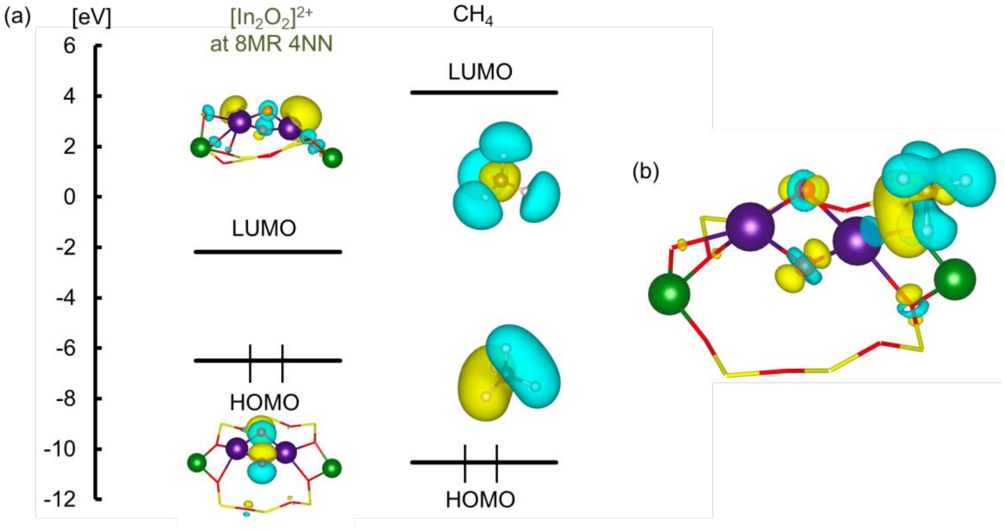

Figure 14. (a) Molecular orbitals of $[In_2O_2]^{2+}$-8MR(4NN) and CH_4. Only selected orbitals are depicted for clarity. (b) Isosurface plot of the charge density difference from isolated CH_4 and $[In_2O_2]^{2+}$-8MR(4NN): yellow, negative charge accumulation; cyan, negative charge depletion.

4. Conclusion

The present study shows that O_2 treatment of In-exchanged CHA zeolites at 773 K affords multinuclear In-oxo clusters that can cleave the C–H bond of CH_4 at mild temperatures. TPR and *in situ* XAFS measurements reveal that the reduced In species are immobilized on CHA through RSSIE and then react with O_2 to form In-oxo clusters. The detailed structure of the In-oxo clusters was predicted by *ab initio* thermodynamics analysis. The obtained phase diagrams indicate that $[In_2O_2]^{2+}$ is the most probable cluster under atmospheric O_2 pressure and dry conditions at the paired Al sites on 8MR. Concerning CH_4 activation, InO_X-CHA activated and oxidized CH_4 at room temperature to afford the adsorbed formic acid, as revealed by *in situ* FT-IR measurements. We also compared the adsorption and activation energies for the C–H bond cleavage of CH_4 over $[In_2O_2]^{2+}$, $[In_4O_4]^{2+}$, and $[In(OH)]^{2+}$ ions formed in the zeolite using DFT calculations, and $[In_2O_2]^{2+}$ was found to be the most active. The molecular orbital analysis revealed that the adsorption of CH_4 is derived from the charge transfer from the HOMO of CH_4 to the LUMO of $[In_2O_2]^{2+}$-8MR(4NN), and the C–H bond cleavage reaction occurs via a heterolytic pathway rather than a homolytic pathway. The creation of multinuclear In-oxo clusters in various zeolites and their application to transformation of CH_4 to higher-value compounds are under investigation.

Conflicts of interest

There are no conflicts to declare.

Acknowledgements

This study was supported financially by a JSPS KAKENHI grant 17H01341, 18K14051 and 18K14057 from the Japan Society for the Promotion of Science (JSPS) and by the Japanese Ministry of Education, Culture, Sports, Science, and Technology (MEXT) within the projects "Integrated Research Consortium on Chemical Sciences (IRCCS)" and "Elements Strategy Initiative to Form Core Research Center", as well as by the JST-CREST projects JPMJCR17J3, JPMJCR15P4 and JST-PREST project JPMJPR16S8. The authors are indebted to the technical division of the Institute for Catalysis (Hokkaido University) for manufacturing experimental equipment. X-ray absorption measurements were performed at the BL-01B1 and BL-14B2 facilities of SPring-8 at the Japan Synchrotron Radiation Research Institute (JASRI) (No. 2018B1126 and 2018B1568). Part of the calculations was performed on supercomputers at RCCS (Okazaki), RIIT (Kyushu Univ.), and ACCMS (Kyoto Univ.).

Note and references

1 J. B. Moffat, *Metal-oxygen clusters: the surface and catalytic properties of heteropoly oxometalates*, Springer Science & Business Media, 2006.
2 C. L. Hill and C. M. Prosser-McCartha, *Coord. Chem. Rev.*, 1995, **143**, 407–455.
3 S.-S. Wang and G.-Y. Yang, *Chem. Rev.*, 2015, **115**, 4893–4962.
4 A. Gunay and K. H. Theopold, *Chem. Rev.*, 2010, **110**, 1060–1081.
5 S. Hayashi, N. Sasaki, S. Yamazoe and T. Tsukuda, *J. Phys. Chem. C*, 2018, **122**, 29398–29404.
6 I. A. Weinstock, E. M. G. Barbuzzi, M. W. Wemple, J. J. Cowan, R. S. Reiner, D. M. Sonnen, R. A. Heintz, J. S. Bond and C. L. Hill, *Nature*, 2001, **414**, 191–195.
7 N. I. Gumerova and A. Rompel, *Nat. Rev. Chem.*, 2018, **2**, 112.
8 S. Ishikawa, Z. Zhang and W. Ueda, *ACS Catal.*, 2018, **8**, 2935–2943.
9 L. Liu, Z. Ji, W. Zou, X. Gu, Y. Deng, F. Gao, C. Tang and L. Dong, *ACS Catal.*, 2013, **3**, 2052–2061.
10 Y. Kamiya, T. Okuhara, M. Misono, A. Miyaji, K. Tsuji and T. Nakajo, *Catal. Surv. from Asia*, 2008, **12**, 101–113.
11 S. Polarz, B. Smarsly, C. Göltner and M. Antonietti, *Adv. Mater.*, 2000, **12**, 1503–1507.
12 R. Rousseau, D. A. Dixon, B. D. Kay and Z. Dohnálek, *Chem. Soc. Rev.*, 2014, **43**, 7664–7680.
13 N. Kosinov, C. Liu, E. J. M. Hensen and E. A. Pidko, *Chem. Mater.*, 2018, **30**, 3177–3198.
14 M. H. Groothaert, P. J. Smeets, B. F. Sels, P. A. Jacobs and R. A. Schoonheydt, *J. Am. Chem. Soc.*, 2005, **127**, 1394–1395.
15 J. S. Woertink, P. J. Smeets, M. H. Groothaert, M. A. Vance, B. F. Sels, R. A. Schoonheydt and E. I. Solomon, *Proc. Natl. Acad. Sci.*, 2009, **106**, 18908–18913.
16 P. Vanelderen, B. E. R. Snyder, M. L. Tsai, R. G. Hadt, J. Vancauwenbergh, O. Coussens, R. A. Schoonheydt, B. F. Sels and E. I. Solomon, *J. Am. Chem. Soc.*, 2015, **137**, 6383–6392.
17 S. Grundner, M. A. C. Markovits, G. Li, M. Tromp, E. A. Pidko, E. J. M. Hensen, A. Jentys, M. Sanchez-Sanchez and J. A. Lercher, *Nat. Commun.*, 2015, **6**, 1–9.
18 E. J. M. Hensen, E. A. Pidko, N. Rane and R. A. Van Santen, *Angew. Chem. Int. Ed.*, 2007, **46**, 7273–7276.
19 E. A. Pidko, R. A. van Santen and E. J. M. Hensen, *Phys. Chem. Chem. Phys.*, 2009, **11**, 2893–1902.
20 C. Hammond, M. M. Forde, M. H. Ab Rahim, A. Thetford, Q. He, R. L. Jenkins, N. Dimitratos, J. A. Lopez-Sanchez, N. F. Dummer, D. M. Murphy, A. F. Carley, S. H. Taylor, D. J. Willock, E. E. Stangland, J. Kang, H. Hagen, C. J. Kiely and G. J. Hutchings, *Angew. Chem. Int. Ed.*, 2012, **51**, 5129–5133.
21 J. Shan, W. Huang, L. Nguyen, Y. Yu, S. Zhang, Y. Li, A. I. Frenkel and F. Tao, *Langmuir*, 2014, **30**, 8558–8569.
22 N. V. Beznis, B. M. Weckhuysen and J. H. Bitter, *Catal. Lett.*, 2010, **136**, 52–56.
23 F. M. Toma, A. Sartorel, M. Iurlo, M. Carraro, P. Parisse, C. MacCato, S. Rapino, B. R. Gonzalez, H. Amenitsch, T. Da Ros, L. Casalis, A. Goldoni, M. Marcaccio, G. Scorrano, G. Scoles, F. Paolucci, M. Prato and M. Bonchio, *Nat. Chem.*, 2010, **2**, 826–831.
24 T. Toyao, N. Ueno, K. Miyahara, Y. Matsui, T. H. Kim, Y. Horiuchi, H. Ikeda and M. Matsuoka, *Chem. Commun.*, 2015, **51**, 16103–16106.
25 C.-Y. Sun, S.-X. Liu, D.-D. Liang, K.-Z. Shao, Y.-H. Ren and Z.-M. Su, *J. Am. Chem. Soc.*, 2009, **131**, 1883–1888.
26 G. E. Johnson, R. Mitrić, M. Nössler, E. C. Tyo, V. Bonačić-Koutecký and A. W. Castleman, *J. Am. Chem. Soc.*, 2009, **131**, 5460–5470.
27 J. Li, S. Zhou, J. Zhang, M. Schlangen, D. Usharani, S. Shaik and H. Schwarz, *J. Am. Chem. Soc.*, 2016, **138**, 11368–11377.
28 J. Cejka, A. Corma, S. Zones and Editors., *Zeolites And Catalysis: Synthesis, Reactions And Applications.*, Wiley-VCH Verlag GmbH & Co. KGaA, 2010.
29 A. A. Arvidsson, V. P. Zhdanov, P. A. Carlsson, H. Grönbeck and A. Hellman, *Catal. Sci. Technol.*, 2017, **7**, 1470–1477.
30 H. K. Beyer, R. M. Mihályi, C. Minchev, Y. Neinska and V. Kanazirev, *Microporous Mesoporous Mater.*, 1996, **7**, 333–341.

31 H. Solt, F. Lónyi, R. M. Mihályi, J. Valyon, L. B. Gutierrez and E. E. Miro, *J. Phys. Chem. C*, 2008, **112**, 19423–19430.
32 T. Baba, Y. Abe, K. Nomoto, K. Inazu, T. Echizen, A. Ishikawa and K. Murai, *J. Phys. Chem. B*, 2005, **109**, 4263–4268.
33 E. Kikuchi, M. Ogura, I. Terasaki and Y. Goto, *J. Catal.*, 1996, **161**, 465–470.
34 R. M. Mihályi, Z. Schay and Á. Szegedi, *Catal. Today*, 2009, **143**, 253–260.
35 S. S. Arzumanov, I. B. Moroz, D. Freude, J. Haase and A. G. Stepanov, *J. Phys. Chem. C*, 2014, **118**, 14427–14432.
36 A. A. Gabrienko, S. S. Arzumanov, I. B. Moroz, I. P. Prosvirin, A. V. Toktarev, W. Wang and A. G. Stepanov, *J. Phys. Chem. C*, 2014, **118**, 8034–8043.
37 A. M. Beale, F. Gao, I. Lezcano-Gonzalez, C. H. F. Peden and J. Szanyi, *Chem. Soc. Rev.*, 2015, **44**, 7371–7405.
38 J. Song, Y. Wang, E. D. Walter, N. M. Washton, D. Mei, L. Kovarik, M. H. Engelhard, S. Prodinger, Y. Wang, C. H. F. Peden and F. Gao, *ACS Catal.*, 2017, **7**, 8214–8227.
39 G. Kresse and J. Furthmüller, *Phys. Rev. B*, 1996, **54**, 11169–11186.
40 G. Kresse and J. Furthmüller, *Comput. Mater. Sci.*, 1996, **6**, 15–50.
41 P. E. Blöchl, *Phys. Rev. B*, 1994, **50**, 17953–17979.
42 Baerlocher, C.; McCusker, L. B.; van Koningsveld, H. Database of Zeolite Structures; http://www.iza-structure.org/databases/ (accessed Jan 2019).
43 O. Bunău and Y. Joly, *J. Phys. Condens. Matter*, 2009, **21**, 345501.
44 Y. Joly, *Phys. Rev. B - Condens. Matter Mater. Phys.*, 2001, **63**, 125120.
45 G. Li, E. A. Pidko, R. A. Van Santen, C. Li and E. J. M. Hensen, *J. Phys. Chem. C*, 2013, **117**, 413–426.
46 D. R. Stull and H. Prophet, JANAF Thermochemical Data, 2nd ed, U.S. National Bureau of Standards, U.S. EPO, Washington, DC, 1971.
47 M. J. G. Frisch, W. Trucks, H. B. Schlegel, G. E. Scuseria, M. A. Robb, J. R. Cheeseman, G. Scalmani, V. Barone, B. Mennucci, G. A. Petersson, H. Nakatsuji, M. Caricato, X. Li, H. P. Hratchian, A. F. Izmaylov, J. Bloino, G. Zheng and J. L. Sonnenberg, *Gaussian Inc. Wallingford, CT*, 2016.
48 A. D. Becke, *Phys. Rev. A*, 1988, **38**, 3098–3100.
49 C. Lee, W. Ynag and R. G. Parr, *Phys. Rev. B - Condens. Matter Mater. Phys.*, 1988, **37**, 785–789.
50 S. H. Vosko, L. Wilk and M. Nusair, *Can. J. Phys.*, 1980, **58**, 1200–1211.
51 M. H. Mahyuddin and K. Yoshizawa, *Catal. Sci. Technol.*, 2018, **8**, 5875–5885.
52 Q. Zhu, J. N. Kondo, T. Tatsumi, S. Inagaki, R. Ohnuma, Y. Kubota, Y. Shimodaira, H. Kobayashi and K. Domen, *J. Phys. Chem. C*, 2007, **111**, 5409–5415.
53 A. W. Chester and E. G. Derouane, *Zeolite characterization and catalysis: A tutorial*, Springer-Verlag New York Inc.: New York, 2010.
54 A. C. Faro, V. D. O. Rodrigues and J. G. Eon, *J. Phys. Chem. C*, 2011, **115**, 4749–4756.
55 A. Getsoian, U. Das, J. Camacho-Bunquin, G. Zhang, J. R. Gallagher, B. Hu, S. Cheah, J. A. Schaidle, D. A. Ruddy, J. E. Hensley, T. R. Krause, L. A. Curtiss, J. T. Miller and A. S. Hock, *Catal. Sci. Technol.*, 2016, **6**, 6339–6353.
56 M. W. Schreiber, C. P. Plaisance, M. Baumgärtl, K. Reuter, A. Jentys, R. Bermejo-Deval and J. A. Lercher, *J. Am. Chem. Soc.*, 2018, **140**, 4849–4859.
57 A. I. Serykh, *J. Phys. Chem. C*, 2016, **120**, 21436–21440.
58 C. Copéret, D. P. Estes, K. Larmier and K. Searles, *Chem. Rev.*, 2016, **116**, 8463–8505.
59 J. A. J. Pardoe and A. J. Downs, *Chem. Rev.*, 2007, **107**, 2–45.
60 K. Reuter and M. Scheffler, *Phys. Rev. B - Condens. Matter Mater. Phys.*, 2002, **65**, 1–11.
61 S. Li, Y. Wang, T. Wu and W. F. Schneider, *ACS Catal.*, 2018, **8**, 10119–10130.
62 C. Paolucci, A. A. Parekh, I. Khurana, J. R. Di Iorio, H. Li, J. D. Albarracin Caballero, A. J. Shih, T. Anggara, W. N. Delgass, J. T. Miller, F. H. Ribeiro, R. Gounder and W. F. Schneider, *J. Am. Chem. Soc.*, 2016, **138**, 6028–6048.
63 C. Liu, G. Li, E. J. M. Hensen and E. A. Pidko, *ACS Catal.*, 2015, **5**, 7024–7033.
64 L. Chen, H. Falsig, T. V. W. Janssens and H. Grönbeck, *J. Catal.*, 2018, **358**, 179–186.
65 J. H. Lunsford, *Catal. Today*, 2000, **63**, 165–174.
66 N. J. Gunsalus, A. Koppaka, S. H. Park, S. M. Bischof, B. G. Hashiguchi and R. A. Periana, *Chem. Rev.*, 2017, **117**, 8521–8573.
67 M. Ravi, M. Ranocchiari and J. A. van Bokhoven, *Angew. Chem. Int. Ed.*, 2017, **56**, 16464–

16483.
68 P. Schwach, X. Pan and X. Bao, *Chem. Rev.*, 2017, **117**, 8497–8520.
69 K. Narsimhan, V. K. Michaelis, G. Mathies, W. R. Gunther, R. G. Griffin and Y. Román-Leshkov, *J. Am. Chem. Soc.*, 2015, **137**, 1825–1832.
70 R. Palkovits, M. Antonietti, P. Kuhn, A. Thomas and F. Schüth, *Angew. Chem. Int. Ed.*, 2009, **48**, 6909–6912.
71 E. V. Kondratenko, T. Peppel, D. Seeburg, V. A. Kondratenko, N. Kalevaru, A. Martin and S. Wohlrab, *Catal. Sci. Technol.*, 2017, **7**, 366–381.
72 A. I. Olivos-Suarez, A. Szécsényi, E. J. M. Hensen, J. Ruiz-Martinez, E. A. Pidko and J. Gascon, *ACS Catal.*, 2016, **6**, 2695–2981.
73 J. F. Hartwig, *J. Am. Chem. Soc.*, 2016, **138**, 2–24.
74 R. Horn and R. Schlögl, *Catal. Lett.*, 2015, **145**, 23–39.
75 Y. Hou, S. Nagamatsu, K. Asakura, A. Fukuoka and H. Kobayashi, *Commun. Chem.*, 2018, **1**, 41.
76 Z. Liang, T. Li, M. Kim, A. Asthagiri and J. F. Weaver, *Science*, 2017, **356**, 299–303.
77 D. K. Pappas, E. Borfecchia, M. Dyballa, I. A. Pankin, K. A. Lomachenko, A. Martini, M. Signorile, S. Teketel, B. Arstad, G. Berlier, C. Lamberti, S. Bordiga, U. Olsbye, K. P. Lillerud, S. Svelle and P. Beato, *J. Am. Chem. Soc.*, 2017, **139**, 14961–14975.
78 B. L. Farrell, V. O. Igenegbai and S. Linic, *ACS Catal.*, 2016, **6**, 4340–4346.
79 B. Ipek, M. J. Wulfers, H. Kim, F. Göltl, I. Hermans, J. P. Smith, K. S. Booksh, C. M. Brown and R. F. Lobo, *ACS Catal.*, 2017, **7**, 4291–4303.
80 Z. Zuo, P. J. Ramírez, S. D. Senanayake, P. Liu and J. A. Rodriguez, *J. Am. Chem. Soc.*, 2016, **138**, 13810–13813.
81 C. Okolie, Y. F. Belhseine, Y. Lyu, M. M. Yung, M. H. Engelhard, L. Kovarik, E. Stavitski and C. Sievers, *Angew. Chem. Int. Ed.*, 2017, **56**, 13876–13881.
82 A. A. Latimer, A. R. Kulkarni, H. Aljama, J. H. Montoya, J. S. Yoo, C. Tsai, F. Abild-Pedersen, F. Studt and J. K. Nørskov, *Nat. Mater.*, 2017, **16**, 225–229.
83 K. Sugiura, S. Ogo, K. Iwasaki, T. Yabe and Y. Sekine, *Sci. Rep.*, 2016, **6**, 25154.
84 T. M. Duncan and R. W. Vaughan, 1981, **471**, 469–471.
85 A. Oda, T. Ohkubo, T. Yumura, H. Kobayashi and Y. Kuroda, *Inorg. Chem.*, 2019, **58**, 327–338.
86 Y. Tsuji and K. Yoshizawa, *J. Phys. Chem. C*, 2018, **122**, 15359–15381.
87 A. Oda, H. Torigoe, A. Itadani, T. Ohkubo, T. Yumura, H. Kobayashi and Y. Kuroda, *J. Phys. Chem. C*, 2014, **118**, 15234–15241.
88 Y. Nishikawa, H. Ogihara and I. Yamanaka, *ChemistrySelect*, 2017, **2**, 4572–4576.
89 R. B. Dos Santos, R. Rivelino, F. D. B. Mota, A. Kakanakova-Georgieva and G. K. Gueorguiev, *Dalt. Trans.*, 2015, **44**, 3356–3366.
90 M. C. Simons, M. A. Ortuño, V. Bernales, C. A. Gaggioli, C. J. Cramer, A. Bhan and L. Gagliardi, *ACS Catal.*, 2018, **8**, 2864–2869.
91 J. Y. Saillard and R. Hoffmann, *J. Am. Chem. Soc.*, 1984, **106**, 2006–2026.
92 E. A. Pidko, V. B. Kazansky, E. J. M. Hensen and R. A. van Santen, *J. Catal.*, 2006, **240**, 73–84.
93 E. A. Pidko and R. A. Van Santen, *J. Phys. Chem. C*, 2007, **111**, 2643–2655.